https://doi.org/10.5194/egusphere-2023-220
Preprint. Discussion started: 24 February 2023

A microstructure-based parameterization of the effective, anisotropic elasticity tensor of snow, firn, and bubbly ice

Kavitha Sundu[1], Johannes Freitag[2], Kévin Fourteau[1,3], and Henning Löwe[1]

[1]WSL Institute for Snow and Avalanche Research SLF, Davos, Switzerland
[2]Alfred-Wegener-Institut, Helmholtz-Zentrum für Polar- und Meeresforschung, Bremerhaven, Germany
[3]Univ. Grenoble Alpes, CNRS, IRD, Grenoble INP, IGE, 38000 Grenoble, France

Correspondence: H. Löwe (loewe@slf.ch)

Abstract. Quantifying the link between microstructure and effective elastic properties of snow, firn, and bubbly ice is essential for many applications in cryospheric sciences. The microstructure of snow and ice can be characterized by different types of fabrics (crystallographic, geometrical) that gives rise to macroscopically anisotropic elastic behavior. While the impact of the crystallographic fabric has been extensively studied in deep firn, the present work investigates the influence of the geometrical fabric over the entire range of possible volume fractions. To this end we have computed the effective elasticity tensor of snow, firn, and ice by finite element simulations based on 395 X-ray tomography images comprising samples from the laboratory, Alps, Greenland, and Antarctica. We employed a variant of the Eshelby tensor that has been previously utilized for the parametrization of thermal and dielectric properties of snow and utilized Hashin-Shtrikman bounds to capture the nonlinear interplay between density and geometrical anisotropy. From that we derive a closed-form parametrization for all components of the (transverse isotropic) elastic tensor for all volume fractions using 2 fit parameters per tensor component. Finally we used the Thomsen parameter to compare the geometrical anisotropy to the crystallographic anisotropy in bubbly ice. While the geometrical anisotropy is clearly dominating up to ice volume fractions of $\phi \approx 0.7$, a thorough understanding of elasticity in bubbly ice may require a coupled elastic theory that includes geometrical *and* crystallographic anisotropy.

1 Introduction

The elastic modulus is the probably the most fundamental mechanical property of snow, firn or ice and the knowledge of the effective elasticity tensor plays a crucial role in a variety of applications throughout the field of cryospheric sciences. Examples comprise micromechanical modeling of snow compaction (Wautier et al., 2016), fracture propagation in weak layers for slab avalanche release (Gaume et al., 2013; Bobillier et al., 2020), or the interpretation of near-surface (Chaput et al., 2022) or deep firn (Diez and Eisen, 2015; Diez et al., 2015; Schlegel et al., 2019) seismic signatures through the link between wave velocities and elastic moduli.

https://doi.org/10.5194/egusphere-2023-220
Preprint. Discussion started: 24 February 2023

In particular the last example (Schlegel et al., 2019) has stressed the role of elastic anisotropy: The retrieval of elasticity profiles of snow, firn, and ice through seismic waves relies on the assumption of isotropy which constitutes an uncertainty in the inversion method. Snow and firn are however known to be anisotropic, on one hand with respect to ice matrix geometry (e.g. Löwe et al., 2013; Calonne et al., 2015; Leinss et al., 2016; Moser et al., 2020; Montagnat et al., 2020), and on the other hand with respect to crystallographic orientation. While the geometrical fabric in firn is high near the surface due to temperature gradient metamorphism (Montagnat et al., 2020) and decays with depth (Fujita et al., 2014), the crystallographic fabric is low near the surface but increases with depth under densification and flow (e.g. Montagnat et al., 2014; Saruya et al., 2022). Recent work wave propagation measurements on glacier ice (Hellmann et al., 2021) suggests that already at very low porosity the effective elastic (crystallographic) anisotropy of polycrystalline ice is already affected by geometrical effects of the ice (porosity). For snow, the impact of the geometrical anisotropy has been studied (Srivastava et al., 2016) only in a limited range of porosities. Thus a parameterization of the elastic modulus, based on density and geometrical anisotropy for the entire possible range of porosities would constitute a first step towards understanding this concurrent anisotropy probem. This could have immediate applications e.g. for retrieving sub-surface density, elasticity, and anisotropy through seismics using advanced inversion methods (Wu et al., 2022).

The effective elasticity tensor of snow, firn or ice can be directly obtained through numerical homogenization on micro-tomography images. Using the Finite-Element (FE) method, the solution of the static linear elastic equations yield the effective elastic properties via volume averaging. Here it is commonly assumed that the ice matrix is isotropic, polycrystalline ice with known bulk and shear modulus (see Garboczi, 1998; Köchle and Schneebeli, 2014; Wautier et al., 2015). It has been recently confirmed that the effective elastic properties obtained by microstructure based FE agree well with acoustic measurements (Gerling et al., 2017). Though straightforward, the microstructure-based FE approach is computationally expensive and requires the microstructure to be known. Therefore, accurate parametrizations are still highly desirable and presently no parametrization of the effective elastic modulus exist that can be consistently applied without making a restriction to a limited range of volume fractions.

As an alternative to numerical simulations, it is often helpful to consider effective medium theories and rigorous approximations. Rigorous bounds such as Hashin-Shtrikman (HS) bounds (Hashin and Shtrikman, 1962) can be used to approximate the elastic properties of porous materials (Torquato, 1991). Although bounds are widely known to be inaccurate predictors of the elastic properties in absolute value (Roberts and Garboczi, 2002), the HS bounds incorporate the non-linear interplay between structural anisotropy and density (Torquato, 2002b) and they have the correct limiting behavior for small and large volume fractions. These properties can be systematically exploited for constructing more sophisticated parametrizations.

It is the purpose of the present work to derive a parameterization of the effective elasticity tensor of snow, firn, and bubbly ice based on volume fraction and structural anisotropy that can be consistently applied to the entire range of volume fractions. This will be achieved by taking the anisotropic HS bounds (containing no free parameter) as functional starting point and subsequently applying an empirical transformation (containing two fit parameters per tensor component), in order to match observed characteristic features, namely the power law increase of the moduli for high porosities (for snow) and the asymptotic behavior of dilute sphere dispersions (for bubbly ice) in the limit of low porosities.

https://doi.org/10.5194/egusphere-2023-220
Preprint. Discussion started: 24 February 2023

The paper is organized as follows. Section 2 gives a theoretical overview of the elasticity tensor, examines the limitation of existing parameterizations and motivates the methodological idea that underlies the proposed parameterization for the elasticity tensor. Section 3 presents an overview of the 395 tomography samples that were used, and the methods that are employed to calculated correlation functions, fabric tensors, FE simulations, and fitting procedures for estimating the free parameters in the elasticity formulas. In Sect. 4 we show performance of new parameterization, by comparing it with the above-mentioned shortcomings of previous work. Finally we discuss in Sect. 5 the expected interplay between crystallographic and geometrical anisotropy for the elastic modulus for snow, firn, and ice and conclude in Sect. 6.

2 Theoretical background

2.1 The effective elasticity tensor

Snow is a heterogeneous material where the effective, macroscopic properties can be computed by volume averaging over a sufficently large volume, known as respresentative volume element (RVE) (see Hill, 1963; Hashin, 1963; Nemat-Nasser and Hori, 1995; Torquato, 1997; Willis, 1981). The effective (fourth order) elasticity tensor $\boldsymbol{C}$ of a statistically homogenous two-phase composite material is defined by Hooke's law of elasticity as

$$\langle \boldsymbol{\sigma} \rangle = \boldsymbol{C} : \langle \boldsymbol{\varepsilon} \rangle, \tag{1}$$

that relates the volume averaged second-order stress $\langle \boldsymbol{\sigma} \rangle$ and strain tensors $\langle \boldsymbol{\varepsilon} \rangle$. Angular brackets denote volume averaging and : denote double contraction (Torquato, 1997). We consider snow to be a transversely isotropic (TI) material, where the axis of transverse symmetry is chosen as the z-axis perpendicular to the isotropic $x\,y$ plane. The elasticity tensor of a TI material can be described by 5 independent moduli. Using Voigt notation, it can be written (Torquato, 2002a) as a symmetric 6×6 matrix

$$\boldsymbol{C} = \begin{bmatrix} C_{11} & C_{12} & C_{13} & 0 & 0 & 0 \\ C_{12} & C_{11} & C_{13} & 0 & 0 & 0 \\ C_{13} & C_{13} & C_{33} & 0 & 0 & 0 \\ 0 & 0 & 0 & C_{44} & 0 & 0 \\ 0 & 0 & 0 & 0 & C_{44} & 0 \\ 0 & 0 & 0 & 0 & 0 & \frac{1}{2}(C_{11} - C_{12}) \end{bmatrix}, \tag{2}$$

For an isotropic material the number of independent entries reduces to two e.g. the shear modulus $G = C_{44}$ and the P-wave modulus C_{33}. Wherever necessary, the common relations are employed (Torquato, 2002a) to connect to alternative formulations in terms of Youngs modulus E, bulk modulus K, or Poisson ratio ν.

https://doi.org/10.5194/egusphere-2023-220
Preprint. Discussion started: 24 February 2023

To quantify the deviation from elastic isotropy, it is common to use the so called Thomsen parameters ϵ, γ, and δ, which are dimensionless quantities defined as (see Thomsen, 1986)

$$\begin{aligned}\epsilon &= \frac{C_{11} - C_{33}}{2C_{33}} \\ \gamma &= \frac{C_{66} - C_{44}}{2C_{44}} \\ \delta &= \frac{(C_{13} + C_{44})^2 - (C_{33} - C_{44})^2}{2C_{33}(C_{33} - C_{44})}.\end{aligned} \tag{3}$$

For an isotropic material the Thomsen parameters are zero.

2.2 Isotropic parametrizations based on ice volume fraction

2.2.1 Snow: Power law models

For applications, the elastic moduli must be related to accessible parameters of snow. The most common way are empirical parameterizations based on density, or equivalently, ice volume fraction ϕ. Density based parameterization often state a power law (Frolov and Fedyukin, 1998; Sigrist, 2006; Gerling et al., 2017) or exponential relationships (Köchle and Schneebeli, 2014; Scapozza, 2004) to comply with the observed drastic increase of elasticity of snow with increasing density. The different density based parametrizations for low density snow have been compared in many publications (e.g. (Köchle and Schneebeli, 2014). For the purpose of the present paper we choose one example, namely the power-law parameterization from Gerling et al. (2017) as it was derived from FE simulations and experiments. We write the parametrization in the form

$$C_{ij}^{\mathrm{G}}(\phi) = a_{ij}\,\phi^{b_{ij}}, \tag{4}$$

where C_{ij}^{G} are the components of the elasticity tensor, a_{ij} and b_{ij} are the empirical parameters that need to be estimated by fitting experimental data. In Gerling et al. (2017) only the 33 component was computed and led to $a_{33} = 6 \cdot 10^{-10}$ and $b_{33} = 4.6$ for snow with volume fractions in the range $0.1 < \phi < 0.4$.

2.2.2 Firn: Kohnen parametrization

A conceptually similar parametrization, however valid for an entirely different range of ice volume fractions, can be inferred from the parametrization of acoustic wave velocities in firn. Kohnen (1972) has derived an empirical relationship between the S and P wave velocities in (isotropic) firn and the density. By relating wave velocities to the respective elastic moduli via density, the Kohnen relations can be cast into a ice volume fraction based parametrization for the S and P wave modulus (33 and 44 components of the elastic modulus) which are valid in low porosity firn. We rewrite the Kohnen empirical formula in the form

$$C_{ij}^{\mathrm{KOH}}(\phi) = \rho \left[v_{ij}^{\mathrm{ice}} - \alpha_{ij} \left(\frac{1}{\phi} - 1 \right)^{1/\beta_{ij}} \right]^2, \tag{5}$$

with the empirical parameters $\alpha_{33} = 2250\,\mathrm{m\,s^{-1}}$, $\beta_{33} = 1.22$, $\alpha_{44} = 950\,\mathrm{m\,s^{-1}}$, and $\beta_{44} = 1.17$, and the P-wave and S-wave velocities in ice $v_{33}^{\mathrm{ice}} = 3900$ and $v_{44}^{\mathrm{ice}} = 2100$ given in units $\mathrm{m\,s^{-1}}$ (Diez, 2013).

https://doi.org/10.5194/egusphere-2023-220
Preprint. Discussion started: 24 February 2023

2.2.3 Ice: Exact limit for dilute dispersions of spheres

For bubbly ice at very low porosities, the air phase can be commonly described as isolated, nearly spherical bubbles (e.g. Fourteau et al., 2019). This limiting case can be addressed analytically by considering a dilute dispersion of spherical cavities with vanishing stiffness ($K^{\text{air}} = G^{\text{air}} = 0$) in ice. In this limit, the effective elastic modulus $\boldsymbol{C}^{\text{DDS}}$ can be computed exactly (Torquato, 2002a) and, due to isotropy, determined from the effective bulk modulus K^{DDS} and shear modulus G^{DDS} given by

$$\begin{aligned} C_{ij}^{\text{DDS}} &= 3K^{\text{DDS}}(\Lambda_h)_{ij} + 2G^{\text{DDS}}(\Lambda_s)_{ij}, \\ K^{\text{DDS}} &= K^{\text{ice}}\left(1 - \frac{3K^{\text{ice}} + 4G^{\text{ice}}}{4G^{\text{ice}}}(1-\phi)\right), \\ G^{\text{DDS}} &= G^{\text{ice}}\left(1 - \frac{G^{\text{ice}} + H^{\text{ice}}}{H^{\text{ice}}}(1-\phi)\right), \end{aligned} \tag{6}$$

where

$$H^{\text{ice}} \equiv G^{\text{ice}}\left(\frac{3K^{\text{ice}}/2 + 4G^{\text{ice}}/3}{K^{\text{ice}} + 2G^{\text{ice}}}\right). \tag{7}$$

Here Λ_h and Λ_s are the hydrostatic and shear projection tensors, respectively, defined in (Torquato, 2002a, Eq. 13.96 and Eq. 13.97) and C_{33}^{DDS} component is given by $K^{\text{DDS}} + 4G^{\text{DDS}}/3$.

2.3 Anisotropic parametrizations based on ice volume fraction and geometrical fabric

To overcome the restrictive assumption of isotropic parametrizations it is necessary to extend the microstructural description. Cowin (1985) showed that the elasticity tensor of porous materials can be estimated, based on symmetry arguments, from the morphology and the elastic properties of the matrix phase (Moreno et al., 2016). According to Cowin (1985), the elasticity tensor can be determined as a function of Lamè constants of the porous material, λ and μ, volume fraction ϕ and the fabric tensor $\boldsymbol{M}$ which captures the anisotropy of the material (Moreno et al., 2016). For snow this was utilized by Srivastava et al. (2016) who used the Zysset–Curnier formulation (Zysset and Curnier, 1995) to incorporate the fabric tensor. This led to a (orthotropic elastic) formulation of the elasiticy tensor given by

$$\begin{aligned} C_{ij}^{\text{ZC}}(\phi, \boldsymbol{M}) = &\sum_{i=1}^{3} (\lambda + 2\mu)\,\phi^k m_i^{2l} (\boldsymbol{M}_i \otimes \boldsymbol{M}_i) \\ &- \sum_{\substack{i,j=1 \\ i\neq j}}^{3} \lambda'\,\phi^k m_i^l m_j^l (\boldsymbol{M}_i \otimes \boldsymbol{M}_j) \\ &+ \sum_{\substack{i,j=1 \\ i\neq j}}^{3} 2\mu\,\phi^k m_i^l m_j^l (\boldsymbol{M}_i \underline{\otimes} \boldsymbol{M}_j), \end{aligned} \tag{8}$$

Here m_i denotes the i-th eigenvalues of the positive definite fabric-tensor $\boldsymbol{M}$ and $\boldsymbol{M}_i$ is the projector on the corresponding eigenspace. The dependence on the eigenvalues and the ice volume-fraction ϕ are assumed to be of power-law type characterized by the empirical exponents k and l, respectively. The definition of double tensorial product $\boldsymbol{A}\underline{\otimes}\boldsymbol{B}$ is given by (Srivastava et al., 2016).

https://doi.org/10.5194/egusphere-2023-220
Preprint. Discussion started: 24 February 2023

The fit parameters derived in Srivastava et al. (2016) for this model are given by $\lambda = 5.33, \lambda^{'} = 5.27, \mu = 9.54$, $k = 4.69$, and $l = 2.55$.

2.4 Anisotropic Hashin-Shtrikman bounds

An alternative theoretical approach to the anisotropic elasticity of heterogeneous materials can be realized through bounds (Hashin and Shtrikman, 1962; Torquato, 1991). Hashin–Shtrikman (HS) bounds predict the effective elastic properties of porous materials based on volume fraction and microstrucural anisotropy, which is incorporated through n-point correlation functions. This results in tighter bounds over Voigt and Reuss bounds, which are just based on the volume fraction of the material. As the air phase of the snow microstructure has zero elasticity, only the upper bound $[0 \leq \boldsymbol{C} < \boldsymbol{C}^{\mathrm{U}}]$ is meaningful (Roberts and Garboczi, 2002) and it is given by (Torquato, 2002a)

$$\boldsymbol{C}^{\mathrm{U}} = \boldsymbol{C}^{\mathrm{ice}} - (1-\phi)\,\phi\boldsymbol{C}^{\mathrm{ice}} : \boldsymbol{P}^{\mathrm{ice}} : \boldsymbol{C}^{\mathrm{ice}} : [\boldsymbol{I} + \phi\boldsymbol{P}^{\mathrm{ice}} : -\boldsymbol{C}^{\mathrm{ice}}]^{-1}, \tag{9}$$

where $\boldsymbol{C}^{\mathrm{U}}$ represents Hashin-Shtrikman upper bound on effective elastic modulus $\boldsymbol{C}$, the components of the fourth-order identity tensor $\boldsymbol{I}$ is given as $I_{pqrs} = (\delta_{pr}\delta_{qs} + \delta_{ps}\delta_{qr})/2$, ϕ is the volume fractions of ice. The bound involves the elasticity tensor $\boldsymbol{C}^{\mathrm{ice}}$ of ice as the host material, which needs to be isotropic for the derivation of Eq. (9). Such an assumption is consistent with our focus on the geometrical, rather than crystallographic, anisotropy and the use of an isotropic material in our FE simulations (see Sec. 3). The bound thus involves the bulk modulus K^{ice} and shear modulus G^{ice} of ice. The tensor $\boldsymbol{P}^{\mathrm{ice}}$ is the polarization tensor, which incorporates the structural anisotropy through aspect ratio α of the correlation lengths (Torquato, 1997). The tensor $\boldsymbol{P}^{\mathrm{ice}}$ is related to the Eshelby tensor $\boldsymbol{S}^{\mathrm{ice}}$ (Eshelby and Peierls, 1957) of the matrix phase via the relation

$$\boldsymbol{P}^{\mathrm{ice}} = \boldsymbol{S}^{\mathrm{ice}} : [\boldsymbol{C}^{\mathrm{ice}}]^{-1}. \tag{10}$$

The Eshelby tensor (see Sect. A) in the Hashin-Shtrikman bounds accounts for the anisotropic "shape" of the microstructure through the geometrical anisotropy ratio α and is the equivalent of the fabric tensor $\boldsymbol{M}$ in the anisotropic ZC model (see Eq. (8)). A geometrical anisotropy ratio $\alpha > 1$ corresponds to predominant vertical orientation of ice matrix (prolate inclusions), $\alpha < 1$ corresponds to predominant horizontal orientation of ice matrix (oblate inclusions), and α =1 corresponds to isotropic distribution of ice matrix.

2.5 Requirements for a consistent elasticity tensor parameterization

The parametrizations and model presented above are all designed for a specific range of validity. To demonstrate the requirements for a consistent parametrization valid for snow, firn, and ice we provide an overview of all models presented above evaluated by using their free parameters as originally published. Figure 1 shows the C_{33} component as a function of volume fraction for all models. For the formulations including anisotropy, three different anisotropy ratios $\alpha = 0.7, 1, \mathrm{and}\, 1.6$ were evaluated and the corresponding spread in elastic properties is shown as shaded area for these models.

Due to its simple power law dependence on density, the G parametrization (Gerling et al., 2017) exceeds even the modulus of ice (black square for $\phi = 1$). A very similar behavior is found for the isotropic ZC (Srivastava et al., 2016) variant, demon-

https://doi.org/10.5194/egusphere-2023-220
Preprint. Discussion started: 24 February 2023

strating the consistency of G and ZC for low volume fractions but the failure for high volume fraction. In addition ZC shows an influence of anisotropy that increases monotonically with ice volume fraction, which is also unphysical since in the limit of $\phi \rightarrow 1$ the microstructure must tend to an isotropic state. In contrast the U bound correctly approaches the ice limiting value of ice (blue square) while the influence of geometrical anisotropy tends to zero. In addition, the U formulation agrees also in the vicinity of $\phi = 1$ with the prediction of dilute dispersion of spherical (DDS) cavities. In contrast, the agreement of U and DDS for $\phi > 0.8$ with the isotropic Kohnen formulation demonstrates the validity of this asymptotic behavior for ice, while in turn KOH naturally fails for low volume fractions (snow) lying outside its range of applicability.

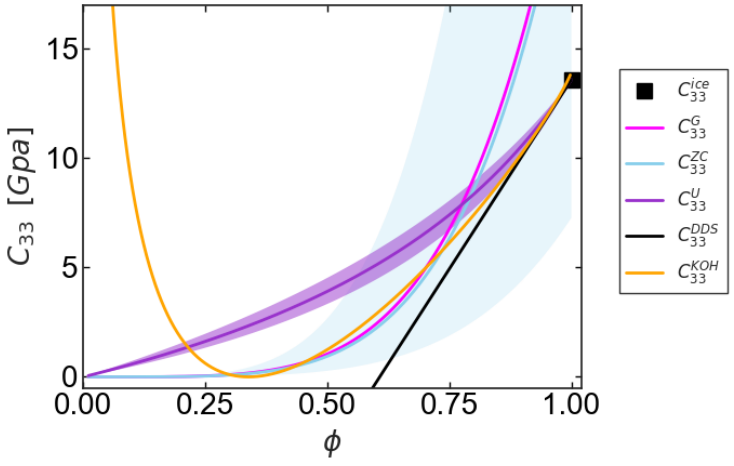

Figure 1. Illustration of the elastic modulus C_{33} as a function of volume fraction ϕ for all discussed models: density based parameterization proposed by Gerling et al. (2017) (C_{33}^{G}) (see Eq. (4)), band of values (C_{33}^{ZC}) predicted by Srivastava et al. (2016) (see Eq. (8)), band of values (C_{33}^{U}) predicted by the Hashin-Shtrikman upper bound (see Eq. (9)), elastic modulus for dilute dispersions (C_{33}^{DDS}) (see Eq. (6)) and for Kohnen (1972) empirical relationship (C_{33}^{KOH}) (see Eq. (5)) are shown as a function of the volume fraction (ϕ) with continuous lines. The black square represents the maximum value of the elastic modulus in C_{33} direction for ice volume fraction $\phi = 1$. The shaded area for the anisotropic models represents the range of values between the two aspect ratios $\alpha = 1.7$ and $\alpha = 0.6$.

2.6 The remedy: Matching asymptotics

The best of all existing models can be combined in a single model by constructing an empirical transition model that i) increases as a power law for low volume fraction ii) includes anisotropy but with vanishing influence when approaching ice iii) approaches the limiting behavior of dilute air bubbles for low porosity. Due to the properties of the HS bounds (correct limiting behavior of the bounds for low and high volume fraction, rational function for intermediate volume fractions) this can

https://doi.org/10.5194/egusphere-2023-220
Preprint. Discussion started: 24 February 2023

be achieved by using a transformation of the normalized HS bound in the following form

$$C_{ij}^{\mathrm{PW}} = C_{ij}^{\mathrm{ice}} f_{ij}\left(\frac{C_{ij}^{\mathrm{U}}}{C_{ij}^{\mathrm{ice}}}\right), \tag{11}$$

with an empirical transition function $f_{ij} : [0,1] \rightarrow [0,1]$ for each component of the elasticity tensor. Given that the HS bound approaches the dilute dispersion limiting behavior for $x \rightarrow 1$ (Hashin and Shtrikman (1962)), the transition functions must obey $f_{ij}(x) \sim x$ for $x \rightarrow 1$. Given further, that the modulus increases as a power law for lower volume fractions, the scaling function must behave as $f_{ij}(x) \sim x^{\beta}$ for $x \rightarrow 0$. These two asymptotics can be matched in the following empirical form

$$f_{ij}(x) = \frac{x^{\beta}}{\xi(1-x)+x^{\beta-1}} \sim \begin{cases} x^{\beta}/\xi, & \text{for } x \rightarrow 0 \\ x, & \text{for } x \rightarrow 1, \end{cases} \tag{12}$$

which has the correct asymptotic behavior and contains only 2 free parameters. The free parameter ξ acts thus on one hand as a modification of the prefactor in the power law and at the same time as the transition scale to control the crossover to $f(x) \sim x$. Eq. (11) and Eq. (12) together with Eq. (9) constitutes our empirical model that depends on density and anisotropy in a physically consistent way. The corresponding tensor components are henceforth referred to as C_{ij}^{PW} which will be analyzed and parametrized in the following from snow, firn, and ice tomography samples and finite element simulations of the elastic modulus.

3 Material and computational methods

3.1 Tomography samples

For the parametrization of snow elastic properties we used 395 microstructure images of snow, firn, and bubbly ice obtained with the help of X-ray tomography (μCT). Samples are taken from previous work and comprise laboratory, Alpine, Arctic, and Antarctic snow and ice. A brief description is given in Table 1. We considered the full range of porosities ranging from 0.06 - 0.93, anisotropy ratios α ranging from 0.45-1.88.

https://doi.org/10.5194/egusphere-2023-220
Preprint. Discussion started: 24 February 2023

Table 1. μCT samples used for the parameterization of the elasticity tensor.

Sample name (No. of. samples)	Description	ϕ range	Anisotropy α range	obtained from
TS-TGM2 (45)	Temperature gradient time series	0.21 - 0.25	0.76 - 1.18	
TS-TGM17 (49)	Temperature gradient time series	0.30 - 0.32	0.90 - 1.15	
TS-DH1 (6)	Metamorphism box time series	0.175 - 0.31	0.74 - 1.45	
TS-DH2 (1)	Metamorphism box time series	0.40	1.575	Löwe et al. (2013)
TS-ISO1 (10)	Isothtermal time series	0.16 - 0.26	0.69 - 1.00	
TS-ISO5 (10)	Isothtermal time series	0.16 - 0.24	0.65 - 1.04	
Alp-DIV (41)	Various Alpine samples	0.06 - 0.39	0.56 - 1.67	
Arc-EGRIP (187)	Snow core	0.24 - 0.66	0.45 - 1.87	Montagnat et al. (2020)
Ant-B34 (4)	Firn core	0.43 - 0.93	1.07 - 1.11	Schlegel et al. (2019)
Ant-B54 (32)	Firn core	0.60 - 0.80	1.00 - 1.17	
Ant-Lock-In (10)	Ice core	0.85 - 0.93	1.05 - 1.12	Fourteau et al. (2019)

3.2 Correlation functions

We use tomography images of snow to compute the correlation functions of snow microstructures to calculate the anisotropy. As dry snow is a two-phase composite material consisting of air and ice phase, the indicator function $\mathcal{I}(\mathbf{x})$ accounts for the spatial distribution of ice and air and is denoted by

$$\mathcal{I}(\boldsymbol{x}) = \begin{cases} 1 & \text{if } \boldsymbol{x} \in \text{ice} \\ 0 & \text{if } \boldsymbol{x} \in \text{air.} \end{cases} \tag{13}$$

The two-point correlation function $\chi(\boldsymbol{r})$ (Torquato, 2002b) entails information about the phase correlation of the end points of vector $\boldsymbol{r}$ and is defined by

$$\chi(\boldsymbol{r}) = \langle \mathcal{I}(\boldsymbol{x}+\boldsymbol{r})\mathcal{I}(\boldsymbol{x})\rangle - \phi^2 \,. \tag{14}$$

We assume a statistically homogeneous material, where χ is independent of the reference point $\boldsymbol{x} \in \mathbb{R}^3$. $\chi(\boldsymbol{r})$ is computed from 3D images via Fast Fourier transformation (Krol and Loewe, 2016; Löwe et al., 2013). Correlation lengths ℓ_z, ℓ_x and ℓ_y are obtained by fitting $\chi_q(\boldsymbol{r})$ along the cartesian coordinate axes $q = x, y$, and z to an exponential function $\chi_q(\boldsymbol{r}) = \chi_{q,0} \exp(-r/\ell_q)$. From this the geometrical anisotropy parameter is defined by $\alpha = \ell_z/\ell_{xy}$.

3.3 Geometrical fabric tensor

Srivastava et al. (2016) showed that the choice of the fabric tensor $\boldsymbol{M}$ computed either by mean intercept lengths (MIL), star length distributions (SLD), and star volume distribution(SVD) methods did not play a significant role in the computation of the

https://doi.org/10.5194/egusphere-2023-220
Preprint. Discussion started: 24 February 2023

effective elasticity tensor of snow. Therefore we use the depolarization tensor $\boldsymbol{M}^*$ given by Torquato (2002a), which is based on two-point correlation lengths to estimate the structural anisotropy of the microstructure. Using $\boldsymbol{M}^*$ allows us to connect to previous work (Löwe et al., 2013; Montagnat et al., 2020; Calonne et al., 2015; Leinss et al., 2016) where this orientation tensor was employed to determine the anisotropic effective thermal conductivity and permittivity of snow. Analogous to MIL, $\boldsymbol{M}^*$ is the symmetric depolarization tensor of a 3-dimensional ellipsoid with the eigenvalues in principle axes frame given by elliptical integrals, and its trace is unity (Torquato, 2002a). In the case of transverse isotropy around the z-axis, the depolarization tensor computed from two-point correlation function $\chi(\boldsymbol{r})$ reduces to

$$\boldsymbol{M}^* = \begin{bmatrix} Q(\alpha) & 0 & 0 \\ 0 & Q(\alpha) & 0 \\ 0 & 0 & 1-2Q(\alpha) \end{bmatrix}. \tag{15}$$

The definition of the function $Q(\alpha)$ in terms of anisotropy ratio α is given in Torquato (2002a, Eq. 17.30 and 17.31).

3.4 FEM simulations

FE simulations were performed using the code from Garboczi (1998) on all the CT images to determine the elasticity tensor of the snow microstructure. For these simulations we assumed elastically isotropic ice with a shear modulus $G^{\text{ice}} = 3.52$ GPa and bulk modulus $K^{\text{ice}} = 8.9$ GPa. We performed FE simulations for 5 load states. For each load state we obtain 6 equations by using $\boldsymbol{\sigma} - \boldsymbol{C} : \boldsymbol{\varepsilon} = 0$ in Voigt notation. All equations resulting from all load states are simultaneously solved for the 5 unknown tensor components by using a linear least squares optimization. The obtained values are denoted by C_{ij}^{FEM}.

3.5 Reparametrization of existing models

From the simulations we also reparametrize existing models from Sec. 2. The unknown parameters in the Gerling model (a_{ij} and b_{ij}), Zysset-Curnier model ($\lambda, \lambda^{'}, \mu, k$ and l) and the present model (ξ and β) are obtained by performing least squares regression on the simulated elasticity tensor components against the models from Sect. 2.2. The free parameters of all models were adjusted using a log-transformation of the elastic tensor component, as it was done in (see Srivastava et al., 2016; Zysset, 2003).

4 Results

4.1 Present study parameterization

Figure 2 shows an overview of all results by plotting the simulated elasticity components C_{ij}^{FEM} (different rows) against ice volume fraction (column 1), the HS upper bound (column 2) and the normalized representation from Eq. (11). This shows that the scatter of the simulated elasticity tensor components (C_{ij}^{FEM}) is maximal when plotted as a function of the ice volume fraction ϕ, and that this scatter is reduced when plotted as a function of the HS upper bound C_{ij}^{U} instead .

https://doi.org/10.5194/egusphere-2023-220
Preprint. Discussion started: 24 February 2023

Next, we use the the improved correlation between C_{ij}^{FEM} and C_{ij}^{U} to derive the parameterizations for each component according to Eq. (12), shown as the black curves. Note that the non-linear transition behavior from the power law increase at low densities when approaching the value of ice is well captured for all the components. The performance however slightly differs for individual tensor components and is the best for C_{33}. We also stress that the data collapse for all tensor components in the normalized plot indicates that only two parameters are sufficient to obtain a decent picture of elasticity from Eq. (11).

https://doi.org/10.5194/egusphere-2023-220
Preprint. Discussion started: 24 February 2023

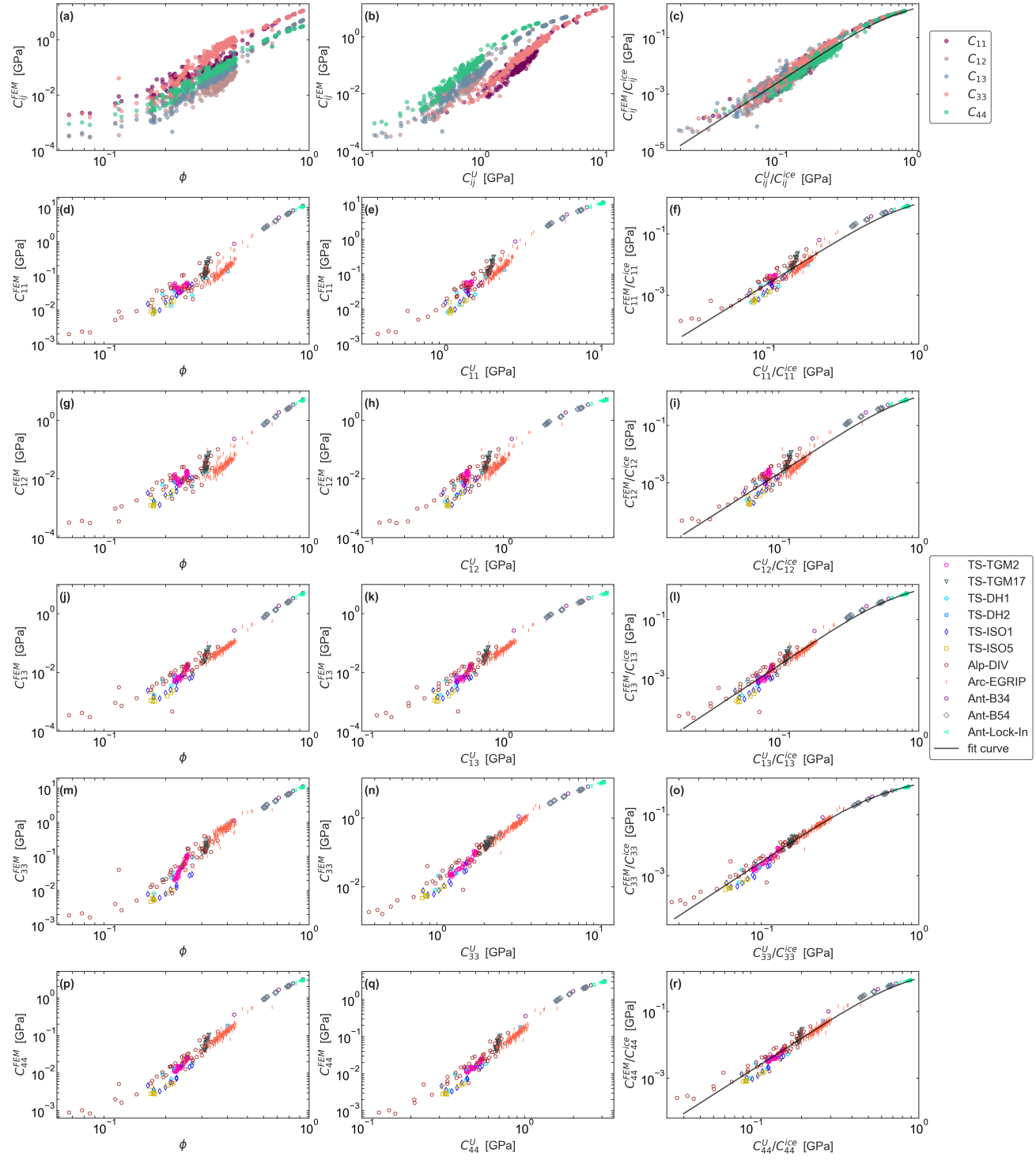

Figure 2. Simulated elasticity components C_{ij}^{FEM} (different rows) are shown as a function of volume fraction ϕ (left column), as a function of HS upper bound C_{ij}^{U} (middle column) and in the normalized version $C_{ij}^{\mathrm{U}}/C_{ij}^{\mathrm{ice}}$ (right column). The black curve represents the parameterization derived for all the components (2 parameters each). For definitions of sample names, we refer to Table 1.

https://doi.org/10.5194/egusphere-2023-220
Preprint. Discussion started: 24 February 2023

4.2 Comparison to previous parameterizations

To examine the performance of the parameterization derived by fitting either individual components (see Fig. 3 top row) or fitting all the components of elastic modulus simultaneously (see Fig. 3 bottom row), we show a scatter plot of the C_{33} component of the elastic modulus evaluated from numerical simulations vs. the three parameterizations: density-based from Gerling (left), Zysset-curnier (middle) and the present study parameterization (right). A detailed overview of the parameters obtained for different parameterization and their coefficient of regression is given in Table 2. Note that these parameters differ from the values obtained in the original publication as the models were re-adjusted to fit our FEM simulations as explained in Sec. 3.5.

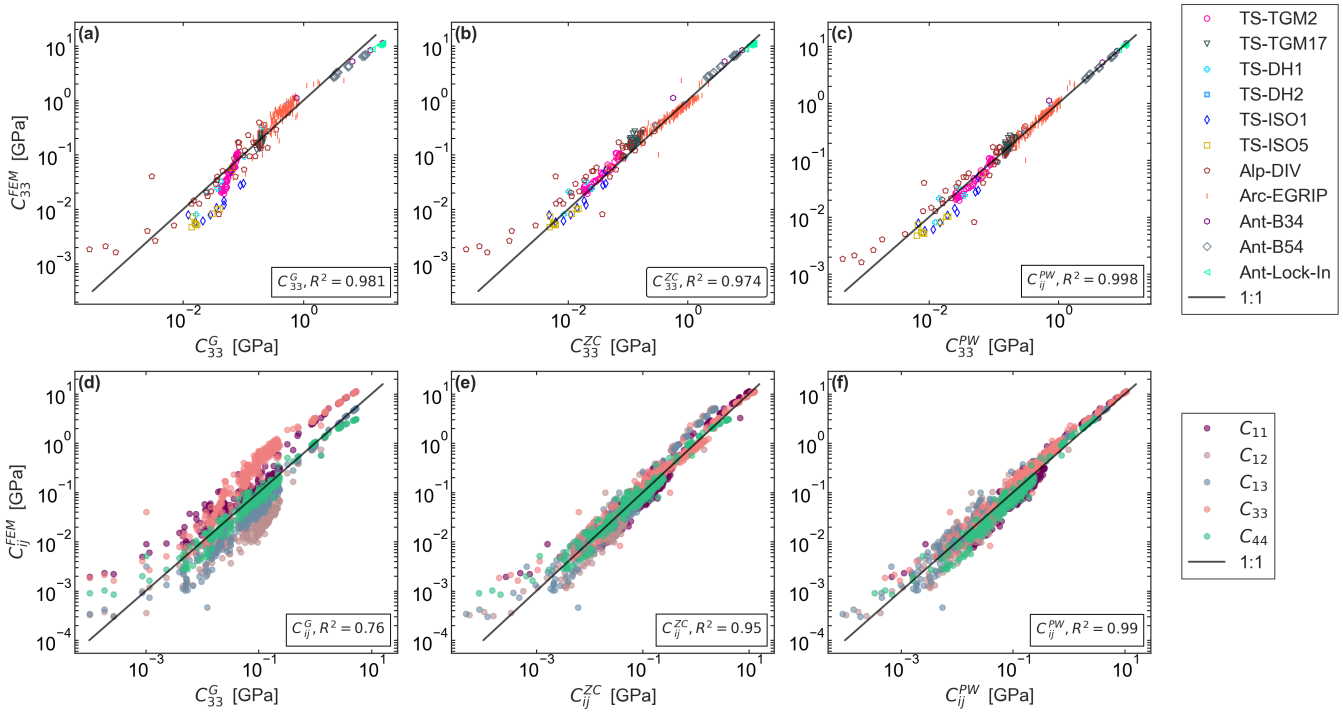

Figure 3. Comparison of simulated elastic modulus (C_{33}^{FEM}) to the Gerling et al. (2017) (G) density-based power law model given by Eq. (4), Zysset-curnier (ZC) model Srivastava et al. (2016) given by Eq. (8) and presentwork parameterization (PW) given by Eq. (12) (from left to right). The given R^2 values correspond to the performance of the parameterization by fitting individual (top) or all components (bottom), respectively. Table 1 provides detailed definitions of sample names.

https://doi.org/10.5194/egusphere-2023-220
Preprint. Discussion started: 24 February 2023

Table 2. Parameters and regression coefficient obtained from least-square regression of the simulated elastic modulus employing different models on the entire data set.

Isotropic parameterization fitted for all components Gerling et al. (2017)			
	a_{ij}	b_{ij}	R^2
C_{ij}^{G}	7.01	4.13	0.76
Isotropic parameterization fitted for each component (Gerling et al., 2017)			
	a_{ij}	b_{ij}	R^2
C_{11}^{G}	8.61	3.82	0.993
C_{12}^{G}	2.86	4.22	0.997
C_{13}^{G}	5.32	4.46	0.997
C_{33}^{G}	27.47	4.26	0.980
C_{44}^{G}	1.34	3.88	0.978
Zysset-Curnier parameterization (Srivastava et al., 2016)			
	λ	$\lambda^{'}$	μ
C_{ij}^{ZC}	0.66	0.21	0.19
	k	l	R^2
C_{ij}^{ZC}	4.08	-1.18	0.952
the present study parameterization fitted for all components			
	β	ξ	R^2
C_{ij}^{PW}	3.07	0.405	0.991
the present study parameterization fitted for individual components			
	β	ξ	R^2
C_{11}^{PW}	3.07	0.49	0.988
C_{12}^{PW}	3.05	0.45	0.988
C_{13}^{PW}	3.12	0.30	0.996
C_{33}^{PW}	3.32	0.18	0.998
C_{44}^{PW}	3.15	0.46	0.992

https://doi.org/10.5194/egusphere-2023-220
Preprint. Discussion started: 24 February 2023

4.3 Comparison at high ice volume fractions

The improvement of the prediction of the elastic modulus using the present work parameterization C_{33}^{PW} at high-volume fraction is compared with elastic modulus determined by Kohnen (1972) formula, where the P-wave velocity of ice $v_{\mathrm{p}}^{\mathrm{ice}}$ is once calculated by using geometrical elastic modulus of ice ($v_{\mathrm{p}}^{\mathrm{ice}} = (C_{33}^{\mathrm{ice}}/\rho^{ice})^{0.5}$) and with the literature P-wave velocity of ice $v_{\mathrm{p}}^{\mathrm{ice}}$ = 3900 ms^{-1} (Diez, 2013). This comparison is depicted in Fig. 4. We see that C_{33}^{KOH} based on the elastic modulus of ice used in this work exactly approaches the correct limit, and is in line with our parameterization C_{33}^{PW} and the limit of elastic modulus for bubbly ice C_{33}^{DDS}. This validity of the C_{33}^{PW}, C_{33}^{KOH}, and C_{33}^{DDS} parametrization at high density is also confirmed by their agreement with the simulated C_{33}^{FEM} values.

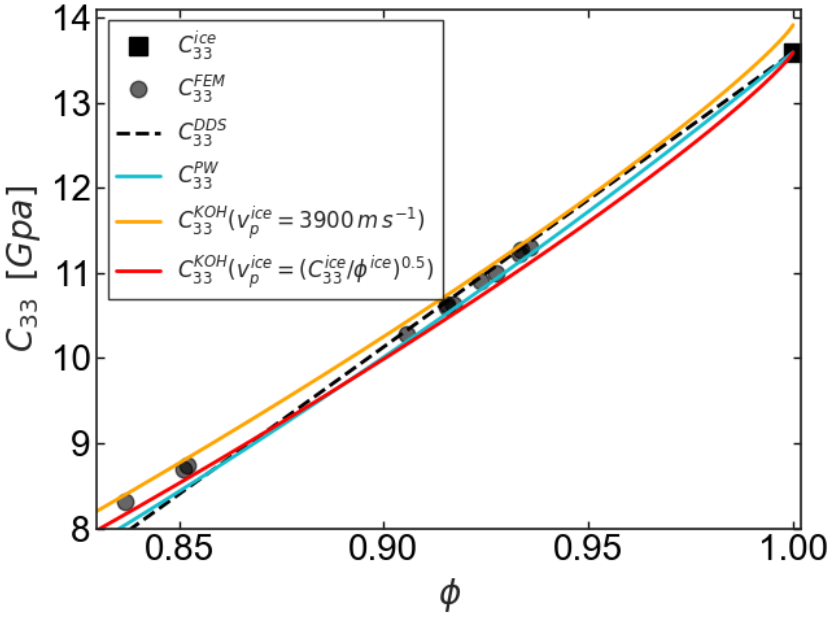

Figure 4. Comparison of present work parameterization C_{33}^{PW} with elastic modulus C_{33}^{KOH} determined by Kohnen (1972) empirical formula based on P-wave velocity and density (P-wave velocity is determined from structural elastic modulus of ice), elastictiy modulus C_{33}^{KOH} obtained by taking P-wave velocity as 3900 ms^{-1} Kohnen (1972) and with upper bound of elastic modulus for dilute dispersion (C_{33}^{DDS}). The black square represents the elastic modulus of ice (C_{33}^{ice}). The black dots correspond to simulations in this density regime (C_{33}^{FEM}).

4.4 Elasticity-depth profile

Another view on the results is provided by comparing the new parametrization to the other parametrizations with their published fit parameters for the only profile (EastGrip) contained in our data. In Fig. 5 the depth-profile of estimated elastic modulus is plotted. The elastic modulus determined from the present work parameterization (C_{33}^{PW}) closely follows the simulated elastic modulus. Conversely the prediction of elastic modulus based on the Kohnen (1972) empirical relationship as a function of P-wave velocities and density cannot be used outside it range of validity (for reasons discussed in Fig. 1). The Gerling et al.

https://doi.org/10.5194/egusphere-2023-220
Preprint. Discussion started: 24 February 2023

(2017) power-law parameterization gives the right prediction only close to the surface where the low anisotropy values $\alpha < 1$ (Montagnat et al., 2020) are consistent with the horizontal anisotropy that was present in the snow samples from (Gerling et al., 2017). For deeper snow the geometrical anisotropy is considerably larger. Note that the volume fraction of Arc-EGRIP microstructure varies from 0.25-0.66. In this range both (C_{33}^{PW}) and (C_{33}^{ZC}) demonstrate a good performance (see Fig. 3) which is also seen in the error-depth profile of elastic modulus depicted in Fig. 5. The error is calculated by $(C_{33}^{\mathrm{FEM}} - C_{33}^{\mathrm{PAR}})/C_{33}^{\mathrm{FEM}}$. Where C_{33}^{PAR} is the parameterization considered for the evaluation of error plot. The error for ZC becomes larger for the highest densities (for reasons discussed in Fig. 1).

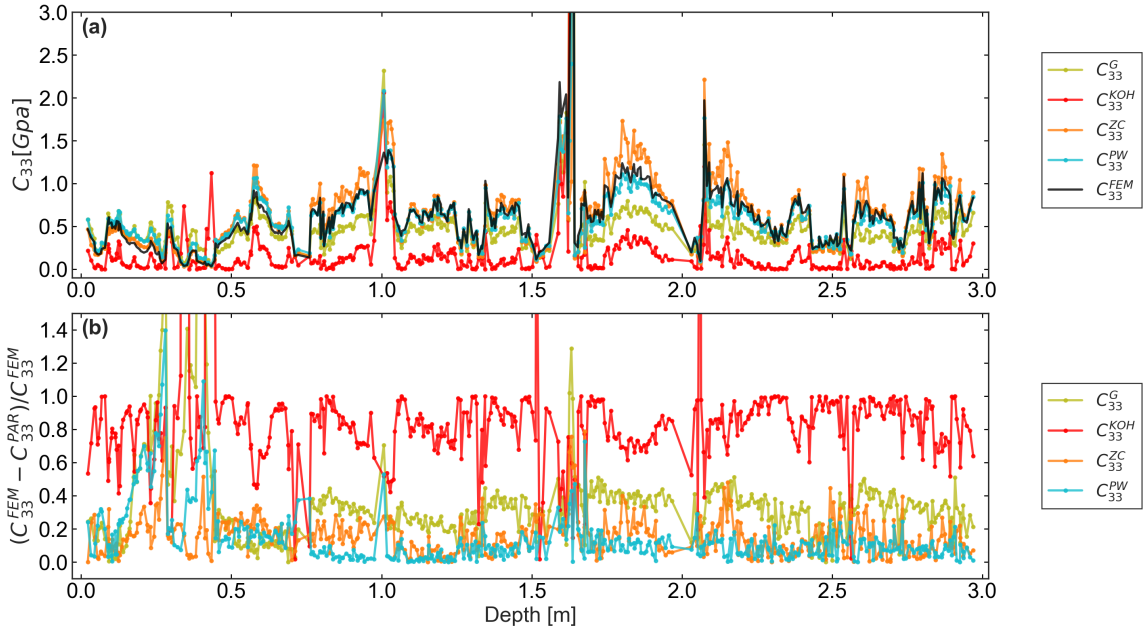

Figure 5. Top: Comparison of elastic modulus calculated from FE simulations for EastGRIP samples to Gerling et al. (2017) parameterization, Kohnen (1972) empirical parameterization, presentwork parameterization, Srivastava et al. (2016) parameterization plotted as a function of depth. Bottom: Error plot which is given by the difference between the simulated elastic modulus C_{33}^{FEM} and parameterized elastic modulus C_{33}^{PAR} normalized by simulated elastic modulus C_{33}^{FEM}.

4.5 Relative influence of geometrical anisotropy and density

While elasticity of snow, firn, and ice is predominantly controlled by density, we can now quantify the additional controls of geometrical anisotropy. To assess the distribution of geometrical anisotropy of the entire data set, we plot structural anisotropy parameter $\alpha = \ell_z/\ell_{xy}$ for all 395 microstrucutures as a function of ice volume fraction in Fig. 6(a). The highest anisotropy parameter ($\alpha = 1.87, \phi = 0.39$) is registered by Arc-EGRIP sample.

The potential error induced by assuming isotropy ($\alpha = 1$) in determining parameterization of elastic modulus is shown in an error plot in Fig. 6 (b). Here the error $(C_{33}^{\mathrm{PW}}(\phi,\alpha) - C_{33}^{\mathrm{PW}}(\phi,1)/C_{33}^{\mathrm{PW}}(\phi,1)$ is shown as a two-dimensional contour plot as a

https://doi.org/10.5194/egusphere-2023-220
Preprint. Discussion started: 24 February 2023

function of ice volume fraction and the anisotropy parameter α. The relative error gives the percentage error induced between the elastic modulus computed as a function of anisotropy and as a function of isotropy, with zero relative error by for isotropic structures.

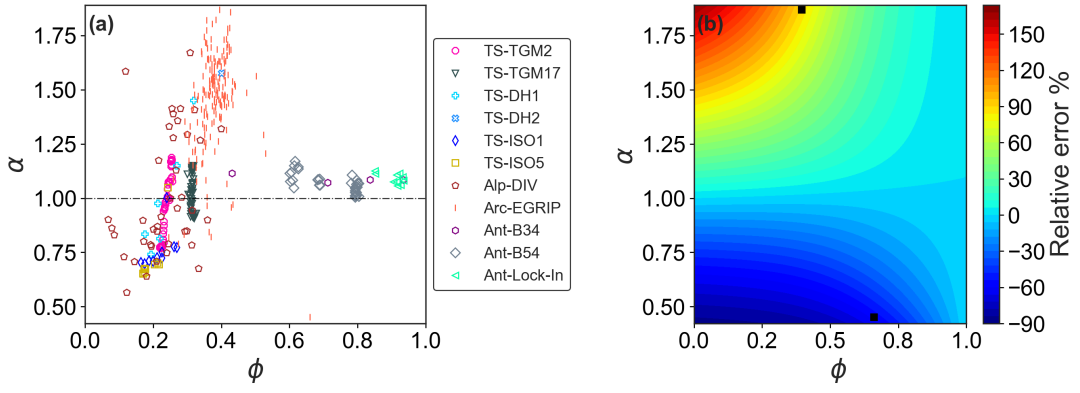

Figure 6. (a): Structural anisotropy of the microstructures (α) is plotted as a function of volume fraction ϕ. Isotropy is represented by dashed line for $\alpha = 1$. (b): Contour plot showing $C_{33}^{\mathrm{PW}}(\phi, \alpha) - C_{33}^{\mathrm{PW}}(\phi, 1)/C_{33}^{\mathrm{PW}}(\phi, 1)$ as a function of anisotropy and volume fraction. The two black squares represents the relative error at the maximum and minimum anisotropy ratio $\alpha = 1.87$ and $\alpha = 0.45$ which occur in the present data set in (a). The bar represents the percentage of relative error computed for different anisotropic microstructures considered. Table 1 provides the description of the samples.

4.6 Comparison of geometrical and crystallographic anisotropy

To assess the geometrical anisotropy in reference to the crystallographic anisotropy when determining the elastic properties of snow, firn, and ice for given ice volume fraction, we show the geometrical Thomsen parameter ϵ_{geom} (see Eq. (3)) in Fig. 7. For comparison we also show the maximum crystallographic anisotropy that can be theoretically obtained, which is the known value of mono-crystalline ice at zero porosity ($\phi = 1$) given by $\epsilon_{\mathrm{cryst}} = -0.0356$ (Petrenko and Whitworth, 1999). The expected (but unknown) decay of $\epsilon_{\mathrm{cryst}}$ for $\phi < 1$ is shown as a schematic (cf. discussion).

https://doi.org/10.5194/egusphere-2023-220
Preprint. Discussion started: 24 February 2023

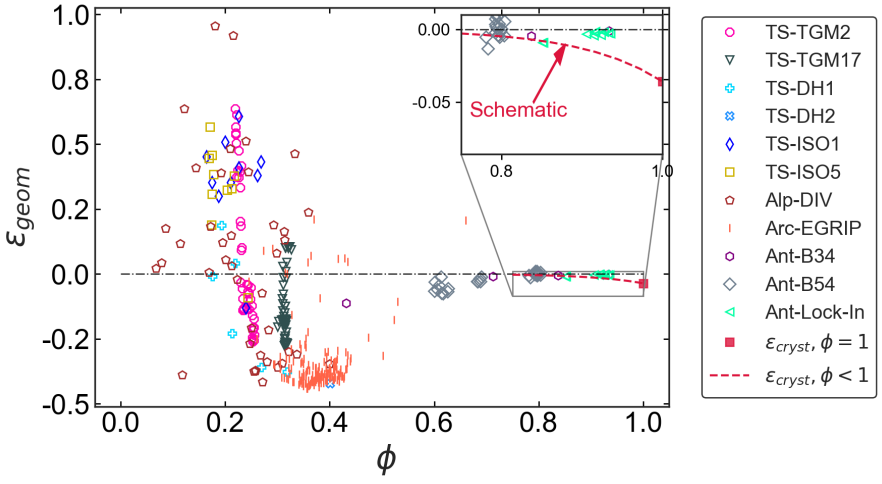

Figure 7. Geometrical and crystallographic Thomsen parameter, ϵ_{geom} and ϵ_{cryst}, plotted as a function of volume fraction ϕ to show the predominant influence of anisotropy (geometrical and crystallographical) on elastic properties. The red dashed line illustrates a schematic representation of the expected behavior of crystallographic anisotropy ϵ_{cryst} for $\phi < 1$. Sample name descriptions are given in Table 1.

5 Discussion

5.1 Summary of main results

The key advantage of the proposed empirical parameterization is the applicability to the entire range of naturally occurring ice volume fraction to predict the effective elastic modulus (see Fig. 3). Previous parametrizations of the elastic modulus, based either on density alone (Eq. (4), Gerling et al. (2017)) or on density and anisotropy (Eq. (8), (Srivastava et al., 2016)), can signifincantly overestimate the elastic modulus when applied outside of their validity range (see Fig. 1). The advantage of HS bound (Eq. (9)) is that it complies with the limiting behavior of bubbly ice (see Sec. 2.6) and does not overestimate the elastic properties as it approaches high volume fraction and incorporates the anisotropy (see Fig. 1). For constructing the empirical parameterization we exploited the fact that the elastic modulus should asymptotically tend to the behavior of randomly diluted spheres, reflecting the fact that low-porosity ice from ice cores mainly consist of convex (sphere like) air cavities (Fourteau et al., 2019). The validity of this assumption is reflected by Fig. 4, which shows that numerical simulations coincide very well with the theoretical prediction of elasticity for dilute dispersions of spherical cavities (see Eq. (6)).

Our parametrization of the elastic modulus is a good alternative to computationally expensive FE methods. Although other theoretical approximations such as the self-consistent (SC) approximation were previously employed by (Wautier et al., 2015) to predict the effective elastic properties and by (Calonne et al., 2019) to predict the effective thermal conductivity for the entire range of densities, SC approximations are based on implicit equations that need to be solved (Torquato, 2002a). Torquato (1998) also showed that the SC give inadequate approximation of effective moduli of dispersions and overestimate the effective moduli in comparison to rigourous bounds. In contrast rigorous bounds such as Hashin-Shtrikman are explicit formulas.

https://doi.org/10.5194/egusphere-2023-220
Preprint. Discussion started: 24 February 2023

It is notable that the range of elastic modulus varies for each tensor component (see Fig.2 (b)) plotted as a function of Hashin-Shtrikman bound. Hence we parameterize elastic modulus for each component shown in Fig. 2 (column 3), as described in Sect. 2.6 using Eq. (12) and the two parameters ξ and β for each component are given in Table 2. We also observed that all five components collapsing onto a single curve when normalizing the simulated values by ice moduli ($C_{ij}^{\mathrm{FEM}}/C_{ij}^{\mathrm{ice}}$) and plotting them as a function of normalized HS upper ($C_{ij}^{\mathrm{U}}/C_{ij}^{\mathrm{ice}}$). This helped in the prediction of all five components of the elastic modulus with only two parameters in contrast to five parameters given by Zysset-curnier parameterization Srivastava et al. (2016) for an orthotropic elasticity tensor.

5.2 Choice of the geometrical fabric tensor

Srivastava et al. (2016) demonstrated that the choice of the fabric tensor does not affect the prediction of anisotropy. Hence the MIL fabric tensor, employed by the Zysset-Curnier parameterization in Srivastava et al. (2016), was replaced here by symmetric depolarization tensor (orientation tensor) $\boldsymbol{M}^*$. In this way, the current elasticity parametrization involves exactly the same microstructure parameter (ϕ, α) as previous permittivity or thermal conductivity parametrizations (Leinss et al., 2016; Löwe et al., 2013). Weng (1992) evaluated bounds using a similar depolarization tensor based on two-point correlation functions assuming ellipsoidal symmetry. Their results were consistent with those of the Hashin-Shtrikman bounds evaluated by Eshelby tensor.

We note that the choice of the fabric tensor though has an impact on the sign of the fit parameter (l) in the Zysset-curnier parameterization, yielding a negative value here in contrast to Srivastava et al. (2016). This can be explained because our depolarization tensor $\boldsymbol{M}^*$ given by Eq. (15) yields a eigenvalue zero in the vertical direction for a vertically oriented microstructure. In contrast, the MIL fabric tensor is represented by $\langle \boldsymbol{m}_i \otimes \boldsymbol{m}_j \rangle$, with a local director $\boldsymbol{m}_i$ and divided by it's trace. If the orientation is in m_i direction then the corresponding eigenvalue in this direction is maximized. Therefore the sign of the l parameter is reversed. A limitation of the MIL fabric tensor is however that it is not able to detect interfacial anisotropy: Odgaard (1997) evaluated a two-dimensional "Swiss cheese" microstructure where the MIL analysis predicted an isotropic geometry despite the obvious, anisotropic arrangement of the spheres. The result of the analysis was influenced by the isotropic interfaces between the phases. Similar results were also observed by Klatt et al. (2017) for a Boolean model, where MIL resulted a circle, with no signatures of anisotropy. MIL determination based on standard line or intersection counting techniques to determine MIL are time consuming and sensitive to noise (Moreno et al., 2012).

5.3 Performance of the parameterization

Overall, our parameterization shows an excellent performance ($R^2 = 0.99$) when fitting all components simultaneously with 2 parameters in comparison to previous parameterizations Srivastava et al. (2016) (volume-fraction and fabric-dependent) and Gerling et al. (2017) (volume-fraction-dependent), which yielded the coefficient of determination $R^2 = 0.76$ and $R^2 = 0.952$, respectively (see Table 2 and Fig. 3). The highest improvement over density based parametrizations is achieved for the C_{33} component for the (TS-TGM2, TS-TGM17, and Arc-EGRIP) samples, which becomes apparent when plotted as a function of HS upper bound or volume fraction (see Fig. 2). All of these samples have an ice matrix predominantly oriented in z-direction

https://doi.org/10.5194/egusphere-2023-220
Preprint. Discussion started: 24 February 2023

(see Fig. 6 (a)) with the anisotropy ratio $\alpha > 1$. Such vertically oriented structures are generated by strong temperature gradient metamorphism (Calonne et al., 2012; Löwe et al., 2013; Leinss et al., 2020) occurring in the snow, firn, and ice. This is evident for temperature gradient time series (TGM2 and MMTO17) from Fig. 6 (a), where we see the change from a horizontal orientation of ice matrix into a vertical orientation. The improvement of the prediction of the elastic modulus mainly in z-direction is consistent with previously derived properties such as thermal conductivity for snow (see, Löwe et al., 2013). EastGRIP (Arc-EGRIP) samples extracted from the firn in Greenland also display similar kind of geometrical anisotropy in the vertical direction (Montagnat et al., 2020).

A possibility to conceptually improve the present parameterization would be to employ additional information of the microstructures e.g. through three-point bounds Torquato (2002a); Roberts and Garboczi (2002); Milton and Phan-Thien (1982). However three-point bounds involve three-point correlation functions which are computationally complex and may still miss relevant details for the estimation of the elastic modulus Beran and Molyneux (1966).

Using the new parametrization it is possible to assess the maximum error in the prediction of elasticity if anisotropy was not taken into account (see Fig. 6(b)). As the relative error is not the same for microstructures with vertical and horizontal orientation of ice matrix, the error plot is non-symmetric in α (see Fig. 6(b)). The relative error of the elastic modulus for vertical ice matrix orientation (TS-TGM2, TS-TGM17 and Arc-EGRIP) $(\alpha > 1)$ (see Fig. 6(b), top half) is larger than 100%. The relative error for horizontal orientation of ice matrix $(\alpha < 1)$ seen for ϕ between snow to ice is up to -90%. From Fig. 6(a) and, 6(b) it is clear that for intermediate volume fractions in the range $0.3 < \phi < 0.5$, very different anisotropy values are possible for a similar density. Using the extreme values from Fig. 6(b) the prediction of elastic modulus solely as a function of ϕ could miss variations up to 200%. For $\phi \to 1$, the relative error must approach zero, since for vanishing porosity (polycrystalline) ice becomes geometrically isotropic.

5.4 Comparison of geometrical and crystallographical anisotropy

In Fig. 6(a) and Fig. 7 we see the typical evolution of the geometrical anisotropy in snow, firn, and ice and its survival up to high densities. Initially, snow exhibits a horizontal orientation of ice matrix (Leinss et al., 2016). As the volume fraction increases from snow to firn, we observe the transition of the orientation to the vertical direction. This change is a result of temperature gradient metamorphism, which can be easily confirmed from the temperature gradient metamorphism experiments (TS-TGM2 and TS-TGM17), and also from the Arc-EGRIP dataset. The existence of geometric anisotropy in polar snow are well known (Fujita et al., 2014; Moser et al., 2020) and can be quantitatively related to temperature gradient metamorphism (Montagnat et al., 2020). When the volume fraction of ice increases further from firn to bubbly ice, the microstructures relax to a geometrically isotropic state. This is a consequence of gravitational settling and densification of snow (Leinss et al., 2020). However we infer from Fig. 6 (a) that the vertical geometrical anisotropy generated near surface survives beyond the bubble close-off transition around $\phi \approx 0.92$ that underlies the Ant-Lock-In data, as disucssed in (Fourteau et al., 2019). This raises the question at which point exactly the crystallographic anisotropy will become the dominant type of anisotropy.

To this end we have quantified the geometrically elastic anisotropy by deriving the corresponding Thomsen parameter ϵ_{geom} for the entire range of ice volume fraction (see Fig. 7). This clearly reveals that the geometrical anisotropy is dominating

https://doi.org/10.5194/egusphere-2023-220
Preprint. Discussion started: 24 February 2023

in snow and firn for ice volume fraction $\phi < 0.7$ in our data. For bubbly ice the situation is a bit more complicated. The crystallographic Thomsen parameter of ice $\epsilon_{\mathrm{cryst}}$ shown in Fig. 7 is only valid for $\phi = 1$, where the geometrical Thomsen parameter ϵ_{geom} must vanish. However, it can be expected that in the range $0.7 < \phi < 1$ the geometrical and crystallographic anisotropy are of similar magnitude since the crystallographic Thomsen parameter $\epsilon_{\mathrm{cryst}}$ must decay from its ice value when increasing the porosity. Such an influence of very low porosity on the crystallographic fabric is also implied by the results of (Hellmann et al., 2021). The expected behavior is shown as a schematic line in the inset of Fig. 7). In principle this curve could be actually computed by assuming a geometrically isotropic air phase (spherical bubbles) in a crystallographically anisotropic ice phase and employing the theoretical work from (Sevostianov et al., 2005). However typos in the equations prevented us from doing so.

For microstructures in the volume fraction range $0.7 < \phi < 1$, it may be thus important in the future to consider concurrent effects of crystallographical and geometrical anisotropy, which is presently inexistent. It is important to know the dominant anisotropy (geometrical or crystallographical) for a given volume fraction for the prediction of elastic properties. Previous studies mostly consider crystallographic anisotropy which may however become dominant only very close to $\phi = 1$

6 Conclusions

Using a transformation of the anisotropic Hashin-Shtrikman bounds, we derived a new closed-form parametrization for the effective elasticity tensor as a function of volume fraction and geometrical anisotropy applicable from fresh snow to bubbly ice. Thereby we extend the set of parameterizations of physical parameters with a similar focus on the full range of volume fractions (Calonne et al., 2019; Picard et al., 2022). We have demonstrated the advantages over previous elasticity parametrizations in view of performance and the correct asymptotic behavior for bubbly ice. Given the distribution of naturally occurring geometrical anisotropy, the uncertainty range of elastic moduli predictions is up to 200% for intermediate volume fractions of $0.3 < \phi < 0.5$ if only density was considered in the parametrization.

The new parametrization constitutes a significant simplification for a use in different applications in cryospheric sciences. In particular we seek to trigger new microstructure retrievals through advanced anisotropic inversion methods of seismic data (Wu et al., 2022). Along these lines, our results shed new light on the relative importance of the two different types of elastic anisotropy (crystallographic, geometrical) in snow and firn that may influence the interpretation of seismic measurements (Schlegel et al., 2019). The geometrical anisotropy is clearly dominating the crystallographic anisotropy for $\phi < 0.7$, and must be taken into account when discussing anisotropy in near surface seismics (Chaput et al., 2022). While the geometrial anisotropy quickly decays with depth, remainders still persists down to the close-off depth and it remains to be investigated in the future how *concurrent* fabrics (geometrical and crystallographic) will elastically interact in bubbly ice.

Data availability. The data will be made available after acceptance.

https://doi.org/10.5194/egusphere-2023-220
Preprint. Discussion started: 24 February 2023

Appendix A: Eshelby tensor

The Eshelby tensor $\boldsymbol{S}$ is defined in terms of elliptical integrals. For the case of a spheroidal inclusion with semi-axis given in terms of correlations lengths $\ell_x = \ell_y = a$ and $\ell_z = b$, with symmetry axis aligned in z-direction embedded in a transverse isotropic comparison phase results in transverse isotropic Eshelby tensor and is defined in terms of with the components of S_{ijkl} given by (Torquato, 2002a; Parnell and Calvo-Jurado, 2015):

$$
\begin{aligned}
S_{1111} = S_{2222} &= \frac{3}{8(1-v_1)}\frac{\alpha^2}{\alpha^2-1} + \frac{1}{4(1-v_1)}\left[1-2v_1-\frac{9}{4(\alpha^2-1)}\right]q,\\
S_{3333} &= \frac{1}{2(1-v_1)}\left\{1-2v_1+\frac{3\alpha^2-1}{\alpha^2-1}-\left[1-2v_1+\frac{3\alpha^2}{\alpha^2-1}\right]q\right\},\\
S_{1122} = S_{2211} &= \frac{1}{4(1-v_1)}\left\{\frac{\alpha^2}{2(\alpha-1)}-\left[1-2v_1+\frac{3}{4(\alpha^2-1)}\right]q\right\},\\
S_{1133} = S_{2233} &= \frac{1}{2(1-v_1)}\left\{\frac{-\alpha^2}{\alpha^2-1}+\frac{1}{2}\left[\frac{3\alpha^2}{\alpha^2-1}-(1-2v_1)\right]q\right\},\\
S_{3311} = S_{3322} &= \frac{1}{2(1-v_1)}\left\{2v_1-1-\frac{1}{\alpha^2-1}+\left[1-2v_1+\frac{3}{2(\alpha^2-1)}\right]q\right\},\\
S_{1212} &= \frac{1}{4(1-v_1)}\left\{\frac{\alpha^2}{2\alpha^2-1}+\left[1-2v_1-\frac{3}{4(\alpha^2-1)}\right]q\right\},\\
S_{1313} = S_{2323} &= \frac{1}{4(1-v_1)}\left\{1-2v_1-\frac{\alpha^2+1}{\alpha^2-1}-\frac{1}{2}\left[1-2v_1-\frac{3(\alpha^2+1)}{\alpha^2-1}\right]q\right\},
\end{aligned}
\tag{A1}
$$

with Poisson ratio of the comparison material given by v_1, α is the aspect ratio of spheroid given in terms of correlation lengths (ℓ_z/ℓ_{xy}) and q is defined by

$$
q = \begin{cases} \dfrac{\alpha}{(\alpha^2-1)^{3/2}}[\alpha(\alpha^2-1)^{1/2} - \cosh^{-1}\alpha], \ \alpha \geq 1, \\ \dfrac{\alpha}{(1-\alpha^2)^{3/2}}[\cos^{-1}\alpha - \alpha(1-\alpha^2)^{1/2}], \ \alpha \leq 1, \end{cases}
\tag{A2}
$$

Several limits of the Eshelby tensor for transverse isotropic materials can be derived. For ice matrix orientation with needle-shaped structures $(\alpha \to \infty, q = 1)$, the Eshelby tensor reads

$$
\begin{aligned}
&S_{1111} = S_{2222} = \frac{5-4v_1}{8(1-v_1)}, S_{3333} = 0\\
&S_{1122} = S_{2211} = \frac{4v_1-1}{8(1-v_1)}, \ S_{1133} = S_{2233} = \frac{v_1}{2(1-v_1)},\\
&S_{3311} = S_{3322} = 0, S_{1212} = \frac{3-4v_1}{8(1-v_1)}, S_{1313} = S_{2323} = \frac{1}{4}.
\end{aligned}
\tag{A3}
$$

For inclusion with disk-shaped structures $(\alpha = 0, q = 0)$, the components of Eshelby are then given by

$$
S_{3333} = 1, S_{3311} = S_{3322} = \frac{v_1}{1-v_1}, S_{1313} = S_{2323} = \frac{1}{2}.
\tag{A4}
$$

https://doi.org/10.5194/egusphere-2023-220
Preprint. Discussion started: 24 February 2023

Author contributions. KS conducted simulations, analyzed the data, created the figures and prepared the manuscript. JF collected the B34/54 data. KF prepared the Lock-in data. HL received the funding, supervised the study, and edited the manuscript.

Competing interests. The authors declare no competing interests.

Acknowledgements. This study was funded by the Swiss National Science Foundation through grant no. 200020_178831.

https://doi.org/10.5194/egusphere-2023-220
Preprint. Discussion started: 24 February 2023

References

Beran, M. and Molyneux, J.: Use of classical variational principles to determine bounds for the effec- tive bulk modulus in heterogeneous media, Quarterly of Applied Mathematics, 24, 107–118, http://www.jstor.org/stable/43635591, 1966.

Bobillier, G., Bergfeld, B., Capelli, A., Dual, J., Gaume, J., van Herwijnen, A., and Schweizer, J.: Micromechanical modeling of snow failure, The Cryosphere, 14, 39–49, https://doi.org/10.5194/tc-14-39-2020, https://tc.copernicus.org/articles/14/39/2020/, 2020.

Calonne, N., Geindreau, C., Flin, F., Morin, S., Lesaffre, B., Roscoat, S. R. D., and Charrier, P.: 3-D image-based numerical computations of snow permeability: links to specific surface area, density, and microstructural anisotropy, The Cryosphere, 6, 939–951, 2012.

Calonne, N., Flin, F., Lesaffre, B., Dufour, A., Roulle, J., Puglièse, P., Philip, A., Lahoucine, F., Geindreau, C., Panel, J.-M., du Roscoat, S. R., and Charrier, P.: CellDyM: A room temperature operating cryogenic cell for the dynamic monitoring of snow metamorphism by time-lapse X-ray microtomography, Geophysical Research Letters, 42, 3911–3918, https://doi.org/https://doi.org/10.1002/2015GL063541, https://agupubs.onlinelibrary.wiley.com/doi/abs/10.1002/2015GL063541, 2015.

Calonne, N., Milliancourt, L., Burr, A., Philip, A., Martin, C. L., Flin, F., and Geindreau, C.: Thermal Conductivity of Snow, Firn, and Porous Ice From 3-D Image-Based Computations, Geophysical Research Letters, 46, 13 079–13 089, https://doi.org/https://doi.org/10.1029/2019GL085228, https://agupubs.onlinelibrary.wiley.com/doi/abs/10.1029/2019GL085228, 2019.

Chaput, J., Aster, R., Karplus, M., and Nakata, N.: Ambient high-frequency seismic surface waves in the firn column of central west Antarctica, Journal of Glaciology, 68, 785–798, https://doi.org/10.1017/jog.2021.135, 2022.

Cowin, S. C.: The relationship between the elasticity tensor and the fabric tensor, Mechanics of Materials, 4, 137 – 147, https://doi.org/https://doi.org/10.1016/0167-6636(85)90012-2, http://www.sciencedirect.com/science/article/pii/0167663685900122, 1985.

Diez, A.: Effects of cold glacier ice crystal anisotropy on seismic data, Ph.D. thesis, http://digbib.ubka.uni-karlsruhe.de/volltexte/1000037984, 2013.

Diez, A. and Eisen, O.: Seismic wave propagation in anisotropic ice - Part 1: Elasticity tensor and derived quantities from ice-core properties, The Cryosphere, 9, 367–384, https://doi.org/10.5194/tc-9-367-2015, http://www.the-cryosphere.net/9/367/2015/, 2015.

Diez, A., Eisen, O., Hofstede, C., Lambrecht, A., Mayer, C., Miller, H., Steinhage, D., Binder, T., and Weikusat, I.: Seismic wave propagation in anisotropic ice - Part 2: Effects of crystal anisotropy in geophysical data, The Cryosphere, 9, 385–398, https://doi.org/10.5194/tc-9-385-2015, 2015.

Eshelby, J. D. and Peierls, R. E.: The determination of the elastic field of an ellipsoidal inclusion, and related problems, Proceedings of the Royal Society of London. Series A. Mathematical and Physical Sciences, 241, 376–396, https://doi.org/10.1098/rspa.1957.0133, https://royalsocietypublishing.org/doi/abs/10.1098/rspa.1957.0133, 1957.

Fourteau, K., Martinerie, P., Faïn, X., Schaller, C. F., Tuckwell, R. J., Löwe, H., Arnaud, L., Magand, O., Thomas, E. R., Freitag, J., Mulvaney, R., Schneebeli, M., and Lipenkov, V. Y.: Multi-tracer study of gas trapping in an East Antarctic ice core, Cryosphere, 13, 3383–3403, https://doi.org/10.5194/tc-13-3383-2019, 2019.

Frolov, A. D. and Fedyukin, I. V.: Elastic properties of snow-ice formations in their whole density range, Annals of Glaciology, 26, 55–58, https://doi.org/10.3189/1998AoG26-1-55-58, 1998.

Fujita, S., Hirabayashi, M., Goto-Azuma, K., Dallmayr, R., Satow, K., Zheng, J., and Dahl-Jensen, D.: Densification of layered firn of the ice sheet at NEEM, Greenland, Journal of Glaciology, 60, 905–921, https://doi.org/10.3189/2014JoG14J006, 2014.

https://doi.org/10.5194/egusphere-2023-220
Preprint. Discussion started: 24 February 2023

Garboczi, E. J.: Finite element and finite difference programs for computing the linear electrical and elastic properties of digital images of random material,NISTIR 6269, US Department of Commerce, 1998.

Gaume, J., Chambon, G., Eckert, N., and Naaim, M.: Influence of weak-layer heterogeneity on snow slab avalanche release: application to the evaluation of avalanche release depths, Journal of Glaciology, 59, 423–437, https://doi.org/10.3189/2013JoG12J161, 2013.

Gerling, B., Löwe, H., and van Herwijnen, A.: Measuring the Elastic Modulus of Snow, Geophysical Research Letters, 44, 11,088–11,096, https://doi.org/https://doi.org/10.1002/2017GL075110, https://agupubs.onlinelibrary.wiley.com/doi/abs/10.1002/2017GL075110, 2017.

Hashin, Z.: Theory of mechanical behavior of heterogeneous media, 1963.

Hashin, Z. and Shtrikman, S.: On some variational principles in anisotropic and nonhomogeneous elasticity, Journal of the Mechanics and Physics of Solids, 10, 335 – 342, https://doi.org/https://doi.org/10.1016/0022-5096(62)90004-2, http://www.sciencedirect.com/science/article/pii/0022509662900042, 1962.

Hellmann, S., Grab, M., Kerch, J., Löwe, H., Bauder, A., Weikusat, I., and Maurer, H.: Acoustic velocity measurements for detecting the crystal orientation fabrics of a temperate ice core, The Cryosphere, 15, 3507–3521, https://doi.org/10.5194/tc-15-3507-2021, https://tc.copernicus.org/articles/15/3507/2021/, 2021.

Hill, R.: Elastic properties of reinforced solids: Some theoretical principles, Journal of the Mechanics and Physics of Solids, 11, 357 – 372, https://doi.org/https://doi.org/10.1016/0022-5096(63)90036-X, http://www.sciencedirect.com/science/article/pii/002250966390036X, 1963.

Klatt, M. A., Schröder-Turk, G. E., and Mecke, K.: Mean-intercept anisotropy analysis of porous media. II. Conceptual shortcomings of the MIL tensor definition and Minkowski tensors as an alternative, Medical Physics, 44, 3663–3675, https://doi.org/https://doi.org/10.1002/mp.12280, https://aapm.onlinelibrary.wiley.com/doi/abs/10.1002/mp.12280, 2017.

Kohnen, H.: Über die Beziehung zwischen seismischen Geschwindigkeiten und der Dichte in Firn und Eis, Zeitschrift für Geophysik. 38(5). Germany, 38, 925, 1972.

Krol, Q. and Loewe, H.: Relating optical and microwave grain metrics of snow: the relevance of grain shape, The Cryosphere, 10, 2847–2863, 2016.

Köchle, B. and Schneebeli, M.: Three-dimensional microstructure and numerical calculation of elastic properties of alpine snow with a focus on weak layers, Journal of Glaciology, 60, 705–713, https://doi.org/10.3189/2014JoG13J220, 2014.

Leinss, S., Löwe, H., Proksch, M., Lemmetyinen, J., Wiesmann, A., and Hajnsek, I.: Anisotropy of seasonal snow measured by polarimetric phase differences in radar time series, The Cryosphere, 10, 1771 – 1797, https://doi.org/10.3929/ethz-b-000121191, 2016.

Leinss, S., Löwe, H., Proksch, M., and Kontu, A.: Modeling the evolution of the structural anisotropy of snow, Cryosphere, 14, 51–75, https://doi.org/10.5194/tc-14-51-2020, 2020.

Löwe, H., Riche, F., and Schneebeli, M.: A general treatment of snow microstructure exemplified by an improved relation for thermal conductivity, The Cryosphere, 7, 1473–1480, https://doi.org/10.5194/tc-7-1473-2013, https://tc.copernicus.org/articles/7/1473/2013/, 2013.

Milton, G. W. and Phan-Thien, N.: New Bounds on Effective Elastic Moduli of Two-Component Materials, Proceedings of the Royal Society of London. Series A, Mathematical and Physical Sciences, 380, 305–331, http://www.jstor.org/stable/2397305, 1982.

Montagnat, M., Azuma, N., Dahl-Jensen, D., Eichler, J., Fujita, S., Gillet-Chaulet, F., Kipfstuhl, S., Samyn, D., Svensson, A., and Weikusat, I.: Fabric along the NEEM ice core, Greenland, and its comparison with GRIP and NGRIP ice cores, The Cryosphere, 8, 1129–1138, https://doi.org/10.5194/tc-8-1129-2014, https://tc.copernicus.org/articles/8/1129/2014/, 2014.

https://doi.org/10.5194/egusphere-2023-220
Preprint. Discussion started: 24 February 2023

Montagnat, M., Löwe, H., Calonne, N., Schneebeli, M., Matzl, M., and Jaggi, M.: On the Birth of Structural and Crystallographic Fabric Signals in Polar Snow: A Case Study From the EastGRIP Snowpack, Frontiers in Earth Science, 8, 365, https://doi.org/10.3389/feart.2020.00365, 2020.

Moreno, R., Borga, M., and Smedby, Ö.: Generalizing the mean intercept length tensor for gray-level images, Medical Physics, 39, 4599–4612, https://doi.org/https://doi.org/10.1118/1.4730502, https://aapm.onlinelibrary.wiley.com/doi/abs/10.1118/1.4730502, 2012.

Moreno, R., Smedby, Ö., and Pahr, D.: Prediction of apparent trabecular bone stiffness through fourth-order fabric tensors, Biomechanics and Modeling in Mechanobiology, 15, 831–844, 2016.

Moser, D. E., Hörhold, M., Kipfstuhl, S., and Freitag, J.: Microstructure of Snow and Its Link to Trace Elements and Isotopic Composition at Kohnen Station, Dronning Maud Land, Antarctica, Frontiers in Earth Science, 8, https://doi.org/10.3389/feart.2020.00023, https://www.frontiersin.org/articles/10.3389/feart.2020.00023, 2020.

Nemat-Nasser, S. and Hori, M.: Universal Bounds for Overall Properties of Linear and Nonlinear Heterogeneous Solids, Journal of Engineering Materials and Technology, 117, 412–432, https://doi.org/10.1115/1.2804735, https://doi.org/10.1115/1.2804735, 1995.

Odgaard, A.: Three-dimensional methods for quantification of cancellous bone architecture, Bone, 20, 315–328, https://doi.org/10.1016/S8756-3282(97)00007-0, 1997.

Parnell, W. and Calvo-Jurado, C.: On the computation of the Hashin-Shtrikman bounds for transversely isotropic two-phase linear elastic fibre-reinforced composites, Journal of Engineering Mathematics, https://doi.org/doi:10.1107/s10665-014-9777-3, 2015.

Petrenko, V. and Whitworth, R.: Physics of Ice, OUP Oxford, https://books.google.ch/books?id=oC941a8lXWIC, 1999.

Picard, G., Löwe, H., and Mätzler, C.: Brief communication: A continuous formulation of microwave scattering from fresh snow to bubbly ice from first principles, The Cryosphere, 16, 3861–3866, https://doi.org/10.5194/tc-16-3861-2022, https://tc.copernicus.org/articles/16/3861/2022/, 2022.

Roberts, A. P. and Garboczi, E. J.: Computation of the linear elastic properties of random porous materials with a wide variety of microstructure, Proceedings of the Royal Society A: Mathematical, Physical and Engineering Sciences, 458, 1033–1054, https://doi.org/10.1098/rspa.2001.0900, 2002.

Saruya, T., Fujita, S., Iizuka, Y., Miyamoto, A., Ohno, H., Hori, A., Shigeyama, W., Hirabayashi, M., and Goto-Azuma, K.: Development of crystal orientation fabric in the Dome Fuji ice core in East Antarctica: implications for the deformation regime in ice sheets, The Cryosphere, 16, 2985–3003, https://doi.org/10.5194/tc-16-2985-2022, https://tc.copernicus.org/articles/16/2985/2022/, 2022.

Scapozza, C.: Entwicklung eines dichte- und temperaturabhängigen Stoffgesetzes zur Beschreibung des visko-elastischen Verhaltens von Schnee, Ph.D. thesis, ETH Zurich, Zürich, https://doi.org/10.3929/ethz-a-004680249, diss., Technische Wissenschaften, Eidgenössische Technische Hochschule ETH Zürich, Nr. 15357, 2004., 2004.

Schlegel, R., Diez, A., Löwe, H., Mayer, C., Lambrecht, A., Freitag, J., Miller, H., Hofstede, C., and Eisen, O.: Comparison of elastic moduli from seismic diving-wave and ice-core microstructure analysis in Antarctic polar firn, Annals of Glaciology, 60, 220–230, https://doi.org/10.1017/aog.2019.10, 2019.

Sevostianov, I., Yilmaz, N., Kushch, V., and Levin, V.: Effective elastic properties of matrix composites with transversely-isotropic phases, International Journal of Solids and Structures, 42, 455–476, https://doi.org/https://doi.org/10.1016/j.ijsolstr.2004.06.047, https://www.sciencedirect.com/science/article/pii/S0020768304003464, micromechanics of Materials, 2005.

Sigrist, C.: Measurement of fracture mechanical properties of snow and application to dry snow slab avalanche release, Ph.D. thesis, ETH Zurich, Zürich, https://doi.org/10.3929/ethz-a-005282374, 2006.

https://doi.org/10.5194/egusphere-2023-220
Preprint. Discussion started: 24 February 2023

Srivastava, P. K., Chandel, C., Mahajan, P., and Pankaj, P.: Prediction of anisotropic elastic properties of snow from its microstructure, Cold Regions Science and Technology, 125, 85 – 100, https://doi.org/https://doi.org/10.1016/j.coldregions.2016.02.002, http://www.sciencedirect.com/science/article/pii/S0165232X16300052, 2016.

Thomsen, L.: Weak elastic anisotropy, GEOPHYSICS, 51, 1954–1966, https://doi.org/10.1190/1.1442051, https://doi.org/10.1190/1.1442051, 1986.

Torquato, S.: Random Heterogeneous Media: Microstructure and Improved Bounds on Effective Properties, Applied Mechanics Reviews, 44, 37–76, https://doi.org/10.1115/1.3119494, https://doi.org/10.1115/1.3119494, 1991.

Torquato, S.: Effective stiffness tensor of composite media—I. Exact series expansions, Journal of the Mechanics and Physics of Solids, 45, 1421 – 1448, https://doi.org/https://doi.org/10.1016/S0022-5096(97)00019-7, http://www.sciencedirect.com/science/article/pii/S0022509697000197, 1997.

Torquato, S.: Effective stiffness tensor of composite media : II. Applications to isotropic dispersions, Journal of the Mechanics and Physics of Solids, 46, 1411 – 1440, https://doi.org/https://doi.org/10.1016/S0022-5096(97)00083-5, http://www.sciencedirect.com/science/article/pii/S0022509697000835, 1998.

Torquato, S.: Random Heterogeneous Materials: Microstructure and Macroscopic Properties, vol. 55, Springer, https://doi.org/10.1115/1.1483342, 2002a.

Torquato, S.: Statistical Description of Microstructures, Annual Review of Materials Research, 32, 77–111, https://doi.org/10.1146/annurev.matsci.32.110101.155324, https://doi.org/10.1146/annurev.matsci.32.110101.155324, 2002b.

Wautier, A., Geindreau, C., and Flin, F.: Linking snow microstructure to its macroscopic elastic stiffness tensor: A numerical homogenization method and its application to 3-D images from X-ray tomography, Geophysical Research Letters, 42, 8031–8041, https://doi.org/https://doi.org/10.1002/2015GL065227, https://agupubs.onlinelibrary.wiley.com/doi/abs/10.1002/2015GL065227, 2015.

Wautier, A., Geindreau, C., and Flin, F.: Numerical homogenization of the viscoplastic behavior of snow based on X-ray tomography images, The Cryosphere, 11, 1465–1485, 2016.

Weng, G.: Explicit evaluation of Willis' bounds with ellipsoidal inclusions, International Journal of Engineering Science, 30, 83 – 92, https://doi.org/https://doi.org/10.1016/0020-7225(92)90123-X, http://www.sciencedirect.com/science/article/pii/002072259290123X, 1992.

Willis, J.: Variational and Related Methods for the Overall Properties of Composites, vol. 21 of *Advances in Applied Mechanics*, pp. 1 – 78, Elsevier, https://doi.org/https://doi.org/10.1016/S0065-2156(08)70330-2, http://www.sciencedirect.com/science/article/pii/S0065215608703302, 1981.

Wu, F., Li, J., Geng, W., and Tang, W.: A VTI anisotropic media inversion method based on the exact reflection coefficient equation, Frontiers in Physics, 10, https://doi.org/10.3389/fphy.2022.926636, https://www.frontiersin.org/articles/10.3389/fphy.2022.926636, 2022.

Zysset, P. and Curnier, A.: An alternative model for anisotropic elasticity based on fabric tensors, Mechanics of Materials, 21, 243 – 250, https://doi.org/https://doi.org/10.1016/0167-6636(95)00018-6, http://www.sciencedirect.com/science/article/pii/0167663695000186, 1995.

Zysset, P. K.: A review of morphology–elasticity relationships in human trabecular bone: theories and experiments, Journal of Biomechanics, 36, 1469 – 1485, https://doi.org/https://doi.org/10.1016/S0021-9290(03)00128-3, http://www.sciencedirect.com/science/article/pii/S0021929003001283, bone Cell and Tissue Mechanics, 2003.